
This is an electronic reprint of the original article.
This reprint may differ from the original in pagination and typographic detail.

Li, Jingrui; Järvi, Jari; Rinke, Patrick

Multiscale model for disordered hybrid perovskites

Published in:
Physical Review B

DOI:
[10.1103/PhysRevB.98.045201](https://doi.org/10.1103/PhysRevB.98.045201)

Published: 03/07/2018

Document Version
Publisher's PDF, also known as Version of record

Please cite the original version:
Li, J., Järvi, J., & Rinke, P. (2018). Multiscale model for disordered hybrid perovskites: The concept of organic cation pair modes. *Physical Review B*, 98(4), 1-13. Article 045201. <https://doi.org/10.1103/PhysRevB.98.045201>

This material is protected by copyright and other intellectual property rights, and duplication or sale of all or part of any of the repository collections is not permitted, except that material may be duplicated by you for your research use or educational purposes in electronic or print form. You must obtain permission for any other use. Electronic or print copies may not be offered, whether for sale or otherwise to anyone who is not an authorised user.

Multiscale model for disordered hybrid perovskites: The concept of organic cation pair modesJingrui Li,^{1,*} Jari Järvi,^{1,2} and Patrick Rinke¹¹*Centre of Excellence in Computational Nanoscience (COMP) and Department of Applied Physics, Aalto University, P.O.Box 11100, FI-00076 AALTO, Finland*²*Department of Physics, University of Helsinki, P.O.Box 64, FI-00014 University of Helsinki, Finland*

(Received 1 April 2017; revised manuscript received 15 May 2018; published 3 July 2018)

We have studied the properties of the prototype hybrid organic-inorganic perovskite $\text{CH}_3\text{NH}_3\text{PbI}_3$ using relativistic density functional theory (DFT). For our analysis we introduce the concept of CH_3NH_3^+ “pair modes,” that is, characteristic relative orientations of two neighboring CH_3NH_3^+ cations. In our previous work [Li and Rinke, *Phys. Rev. B* **94**, 045201 (2016)] we identified two preferential orientations that a single CH_3NH_3^+ cation adopts in a unit cell. The total number of relevant pairs can be reduced from the resulting 196 combinations to only 25 by applying symmetry operations. DFT results of several $2 \times 2 \times 2$ supercell models reveal the dependence of the total energy, band gap, and band structure on the distribution of CH_3NH_3^+ cations and the pair modes. We have then analyzed the pair-mode distribution of a series of $4 \times 4 \times 4$ supercell models with disordered CH_3NH_3^+ cations. Our results show that diagonally oriented CH_3NH_3^+ cations are rare in optimized $\text{CH}_3\text{NH}_3\text{PbI}_3$ supercell structures. In the prevailing pair modes, the C–N bonds of the two neighboring CH_3NH_3^+ cations are aligned approximately vertically. Furthermore, we fit the coefficients of a pair-mode expansion to our supercell DFT reference structures. The pair-mode model can then be used to quickly estimate the energies of disordered perovskite structures. Our pair-mode concept provides combined atomistic-statistical insight into disordered structures in bulk hybrid perovskite materials.

DOI: [10.1103/PhysRevB.98.045201](https://doi.org/10.1103/PhysRevB.98.045201)**I. INTRODUCTION**

Hybrid perovskite photovoltaic (HPPV) technology [1,2] is the most recent rising star in the emerging solar-cell community due to its record increase in power-conversion efficiency (PCE) during the last five years [3]. The current state-of-the-art HPPV architecture was proposed in 2012 achieving $\sim 10\%$ PCE [4,5]. Now the PCE of HPPV cells has already reached 22%, overtaking the best-performing inorganic-based single-junction thin-film cells such as CdTe and copper-indium-gallium-selenide (CIGS) cells [3,6]. The most common photoactive material in HPPV cells is methylammonium ($\text{MA} \equiv \text{CH}_3\text{NH}_3$) lead triiodide ($\text{CH}_3\text{NH}_3\text{PbI}_3$, shortened as MAPbI_3 hereafter). This hybrid perovskite material exhibits several advantageous features for photovoltaic applications, such as a band gap close to the optimal value for single-junction solar-cell absorbers [7], excellent absorption strength in the visible part of the solar spectrum [8], and high mobilities for both electron and hole transport [9,10]. It can be synthesized in solution at low temperature from common starting materials that have limited harm to the environment. Therefore HPPV cells are considered as promising candidates that can offer clean, affordable, and sustainable energy.

Apart from the PCE improvement, recent experimental and theoretical studies in HPPV technology have focused on the origin of the high mobility and low recombination rate [9–12], the observed current-voltage hysteresis [7,13–15], and the stability of hybrid perovskites materials [16–18]. To

resolve open questions in hybrid perovskites it is imperative to develop a comprehensive understanding of their atomic structure, which is both fundamental and challenging due to the structure’s complexity. Taking the prototype hybrid perovskite MAPbI_3 as an example, the central cation MA^+ is not spherical (as, e.g., Cs^+ in the conventional perovskite CsPbI_3) but exhibits polarity and an orientational preference in the lattice. At low temperatures, MAPbI_3 assumes a minimal-energy structure with regularly aligned MA^+ cations and thereby a regularly deformed inorganic PbI_3^- matrix, resulting in an orthorhombic phase. Conversely, at room temperature or above, the MA^+ cations are thought to be randomly oriented due to thermal fluctuations, forming (dynamically) disordered structures [7,19–21].

The detailed mechanism leading to disorder is not yet fully understood. Wasylishen *et al.* [22] claimed that the change of an MA^+ ion’s C–N bond direction (called reorientation hereafter) occurs on a subpicosecond timescale in the cubic phase of MA -based perovskites based on ^{14}N -NMR measurements. Conversely, Poglitsch and Weber (using millimeter-wave spectroscopy) [19], Bakulin *et al.* (two-dimensional infrared vibrational spectroscopy) [23], and Chen *et al.* (quasielastic neutron scattering) [24] reported characteristic times for MA reorientation on a picosecond timescale. For the activation energy of the C–N bond rotation, recent first-principles molecular dynamics (MD) simulations give a value of 42 meV [25], whereas other theoretical [26–29] and also experimental [26,30] studies suggested that it is of the order of 100 meV. Such a discrepancy can lead to significantly different scenarios. A small reorientation energy implies that the MA^+ cations are loosely attached to the inorganic cage and can rotate almost

*jingrui.li@aalto.fi

freely within the lattice at room temperature. This would lead to dynamical three-dimensional isotropy on a length scale of one single cell ($\sim 6 \text{ \AA}$). In contrast, if the activation energy is $\sim 100 \text{ meV}$ (corresponding to $\sim 1200 \text{ K}$), the probability for an MA^+ to overcome such a barrier is very low at room temperature. The MA^+ cations will then remain bound to the inorganic framework via hydrogen bonds [28,31,32] for a relatively long time. In this scenario, localized MA patterns [33–35] would form on short length scales. On large length scales, MAPbI_3 appears effectively cubic.

Modeling the orientational disorder of MA^+ ions in MAPbI_3 is a challenging task. Quantum mechanical first-principles techniques are required to correctly describe the hydrogen bonding of MA^+ ions to the inorganic cage and the corresponding distortions of the cage. However, even density-functional theory (DFT), which in local or semilocal approximations is currently the most computationally efficient first-principles technique, cannot scale up to the required length scales or the large number of candidate structures. The simple primitive-cell model is not representative of MAPbI_3 's atomic structure, as it effectively describes a system of infinitely many aligned polar MA^+ ions. The dipole moment introduced by each MA^+ unit can be canceled by compensating alignments of MA^+ ions in an appropriately chosen supercell model. For such compensated models, the atomic and electronic structure, especially in the low-temperature orthorhombic and tetragonal phases, can then be calculated at the DFT or beyond level by means of small supercell models such as $\sqrt{2} \times \sqrt{2} \times 2$ and $2 \times 2 \times 2$ [26,36–39]. $2 \times 2 \times 2$ supercell models have also been adopted to study the distribution of MA^+ orientations at a finite temperature using *ab initio* MD [34,40]. However, to really model disorder we would need to know the structure of MAPbI_3 on a length scale of a few to a few tens of single (primitive) cells. $2 \times 2 \times 2$ supercell models do not suffice for this purpose because of the periodic boundary conditions, while DFT calculations for larger supercell models become computationally very demanding.

Only recently three studies employed large supercell models to approach the structural complexity [25,41]. Meloni *et al.* [25] used *ab initio* MD to study the time-dependent autocorrelation function of C–N bond directions at different temperatures in a $2\sqrt{2} \times 2\sqrt{2} \times 4$ supercell model, and claimed an activation energy of 42 meV for MA reorientation. Lahnsteiner *et al.* [41] constructed a series of $n \times n \times n$ supercell models with $n = 2, 4, 6$ to model MAPbI_3 at different temperatures. Their results indicate that the C–N bonds are very rarely oriented along the diagonal direction within a single cell, and the angles between the C–N bonds of two MA^+ cations follow certain static and dynamical correlation in the cubic phase. Lahnsteiner *et al.* provide an important reference for our study, especially for the analysis of C–N bond direction and the alignment of MA^+ ions in MAPbI_3 . In addition, they reported that the upper bound for the reorientation of an MA^+ is 7 ps at room temperature. For even larger supercells ($n = 8, 12$), Ma and Wang [42] studied the electronic structure of MAPbI_3 using the *ab initio* three-dimensional fragment method. In their model systems, the C–N bonds were randomly oriented along the diagonal directions of a single cell. Their results indicate that the orientational disorder induce a charge-density localization of both valence-band

maximum and conduction-band minimum on small length scales.

In our previous work [32] we have comprehensively analyzed the atomic structure of hybrid perovskites using the primitive-cell model. We found several stable locations of MA^+ in the lattice. Moreover, our analysis revealed that the stability of hybrid perovskites is closely related to the deformation of the inorganic cage, which acts synergetically with the organic ions analogous to a chicken-and-egg paradox. In this work we performed DFT calculations for a number of different MAPbI_3 supercell models and focus on the pairs of neighboring MA^+ ions. We devised a pair-mode description that reduces each MA^+ ion to a dipole [43] with discrete orientations that were adopted from our previous primitive-cell results [32]. We then defined the relative geometry of two nearest individual dipoles as a “pair mode.” With the pair-mode concept, we were able to relate the dependence of certain MAPbI_3 properties (e.g., total energy, band structure) to the distribution of MA orientations and to the dipoles’ alignment. This was done by studying a series of $2 \times 2 \times 2$ supercell models. We further investigated $4 \times 4 \times 4$ supercell models focusing on the distribution of pair modes. This distribution tells us for a given dipole which dipole orientations are preferred in its surrounding, thus providing knowledge of the local structure beyond a single MAPbI_3 unit cell.

The remainder of this paper is organized as follows. In Sec. II we briefly describe the model systems and the computational details of our DFT calculations. Section III outlines the concept of pair modes, and uses this concept to discuss the results of the supercell models. Finally, Sec. IV concludes with a summary.

II. COMPUTATIONAL DETAILS

The supercell models considered in this paper were constructed based on single (primitive) cells. In each single cell, the MA^+ is located close to the center of the cell, Pb^{2+} at the corners, and I^- at the edge centers. We considered a series of $2 \times 2 \times 2$ and $4 \times 4 \times 4$ supercell models for different purposes. In $2 \times 2 \times 2$ supercell models the total dipole moment can be easily canceled with regular alignments of MA^+ ions. Although a $2 \times 2 \times 2$ supercell model is larger than a $\sqrt{2} \times \sqrt{2} \times 1$ model, it has the advantage that it does not introduce artificial differences between the three lattice directions *a priori*. Compared with the $2 \times 2 \times 2$ counterparts, the larger $4 \times 4 \times 4$ supercell models contain 64 MA^+ cations, thus providing appropriate model systems to mimic the disordered structures by introducing randomly oriented MA^+ ions. The considered supercell models were fully randomly initialized with different MA^+ alignments.

The choice of $4 \times 4 \times 4$ supercell models (containing 768 atoms) is based on the following considerations: (a) The smaller $3 \times 3 \times 3$ supercell models cannot properly host the octahedron tilting of the perovskite structure due to the odd number of single cells along each lattice vector [44]. Nonetheless, we have also studied a series of $3 \times 3 \times 3$ supercells and the results are provided in Sec. S4 of Ref. [59] for comparison. (b) Some smaller supercell models, such as $2\sqrt{2} \times 2\sqrt{2} \times 4$, may introduce artifacts, as they limit the number of possibilities of MA alignments along the two shorter lattice vectors so

that the results would be very sensitive to the random initial geometry of MA^+ ions [41]. (c) Even larger supercell models contain > 1000 atoms and are thus computationally too expensive for conventional DFT modeling.

In our previous study [32] we demonstrated that the “PBE+vdW” exchange-correlation functional produces the lattice constants of hybrid perovskite systems in good agreement with experiment, and can properly describe the interaction between the organic cations and the inorganic framework. Thus we adopted this functional for all DFT calculations in this work. Specifically, the Perdew-Burke-Ernzerhof (PBE) generalized gradient approximation [45] was used as the exchange-correlation functional, and the long-range van der Waals (vdW) interactions were described by employing the Tkatchenko-Scheffler method based on the Hirshfeld partitioning of the electron density [46]. In addition, scalar relativistic effects were included via the zero-order regular approximation (ZORA) [47]. Although spin-orbit coupling [48–51] and exact exchange or many-body corrections [50,52,53] have significant impact on the band structure of MAPbI_3 , we did not include them in the band-structure calculations (for the $2 \times 2 \times 2$ supercell models), since they are computationally very demanding. For the relative differences of band gaps between different supercell models PBE+vdW+ZORA is sufficient.

All calculations were carried out using the all-electron numeric-atom-centered orbital code FHI-AIMS [54–56]. For the $2 \times 2 \times 2$ supercell models, we used a Γ -centered $4 \times 4 \times 4$ k -point mesh and tier 2 basis sets for both structure relaxation and band-structure calculations. We performed direct lattice-vector optimization with the analytical stress tensor implemented in FHI-AIMS [57]. For the larger $4 \times 4 \times 4$ supercells, we have reduced the computational expense by employing a $2 \times 2 \times 2$ k -point mesh and tier 1 basis sets. The geometries were optimized for a fixed size of the cubic unit cell, for which the lattice parameter $a = 25.25 \text{ \AA}$ was adopted based on the experimental value $a_0 = 6.31 \text{ \AA}$ of the primitive cell [7]. The results of all relevant calculations of this work are available from the Novel Materials Discovery (NoMaD) repository [58].

III. RESULTS AND DISCUSSIONS

A. Definition of CH_3NH_3^+ pair modes

The essential difference between conventional perovskites such as CsPbI_3 and hybrid perovskites is the monovalent central cation. Metal cations such as Cs^+ are spherically symmetric, while the polar organic CH_3NH_3^+ cation has a permanent dipole moment pointing from the C end (the methyl group) to the N end (the ammonium cation group). Thus, in a primitive-cell model all MA^+ ions will be aligned parallel. This would result in a large dipole moment in the bulk material, which is not observed experimentally. Supercell models allow us to cancel the total dipole moment in the supercell. In this paper we calculated the total dipole moment within a supercell by the vector sum of individual MA^+ dipole moments (or its average per MAPbI_3 unit) and represent it in terms of p_0 , the permanent dipole moment of an isolated MA^+ in vacuum. Our PBE+vdW/tier 2 result of p_0 is 2.2 D, very close to the B3LYP/6-31G* result of 2.3 D [33].

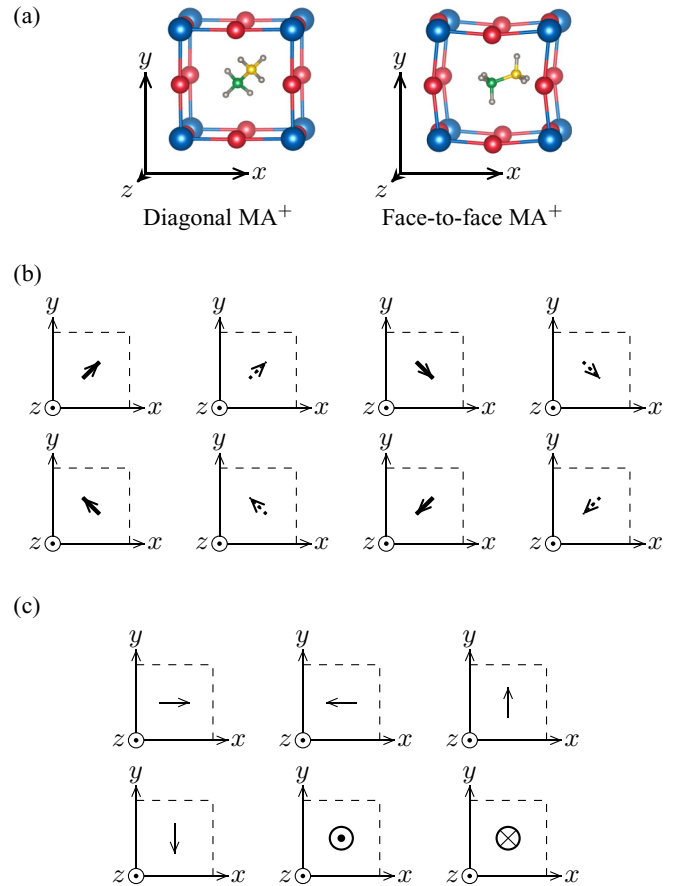


FIG. 1. Symbolic representation of a CH_3NH_3^+ ion by an arrow pointing from C to N. (a) Two stable structures (left: with diagonally oriented MA^+ , and right: with MA^+ oriented approximately along face-to-face) obtained from primitive-cell calculations (data taken from Ref. [32]). C, N, H, Pb, and I atoms are colored in green, yellow, gray, blue, and red, respectively. (b) and (c) Dipole representation for MA^+ along (b) diagonal and (c) face-to-face orientations. \odot and \otimes indicate dipoles that are perpendicular to the plane of the paper and point out of and into it, respectively. Likewise, thick solid arrows in (b) point out of the plane of the paper, while dashed arrows point into the paper.

Our previous DFT calculations [32] revealed two stable structures of the cubic primitive-cell model, as shown in Fig. 1(a). Specifically, in the left structure of Fig. 1(a), the C–N bond is oriented along the diagonal ($[111]$ or equivalent) direction of the single unit cell, while in the right structure it is oriented along the face-to-face ($[100]$ or equivalent) direction with a small deviation. The face-to-face MA^+ structure is 21 meV more stable than the diagonal structure. We attribute this stability to the considerably larger deformation of the inorganic framework in the face-to-face structure. As a side note, the internal atomic geometry of MA^+ in MAPbI_3 is nearly independent of its location in the unit cell.

To simplify our notation, we abstract each MA^+ in the optimized MAPbI_3 structure by an arrow along its C–N bond that represents its dipole moment. Corresponding to the eight diagonal and six face-to-face directions in the cubic single cell, there are altogether 14 possible directions for such a dipole. They are illustrated in Figs. 1(b) and 1(c), respectively.

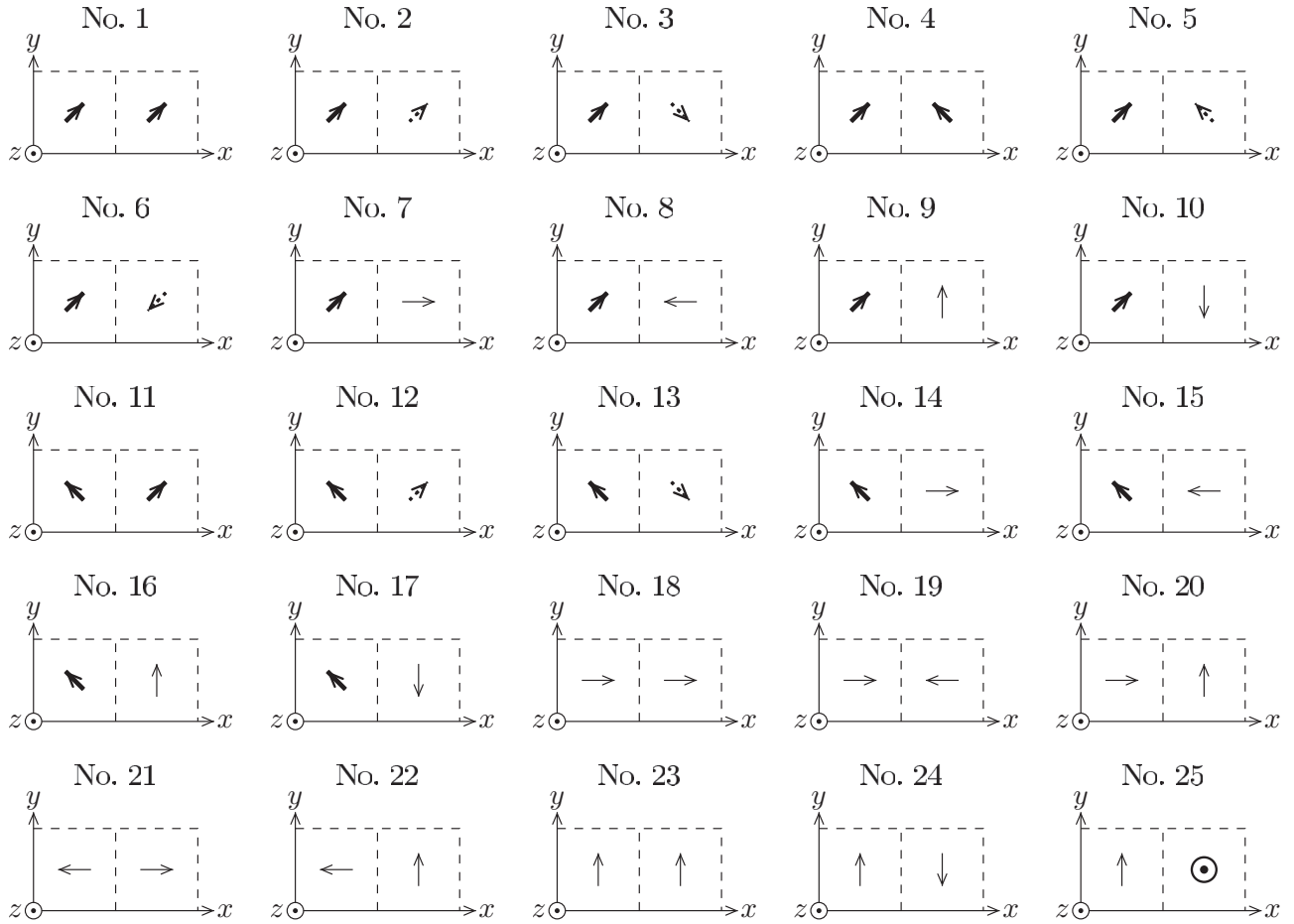


FIG. 2. The 25 pair modes of neighboring MA^+ ions considered in this paper. Each MA^+ ion is represented by arrows indicating the direction from C to N, that is, the direction of the CH_3NH_3^+ dipole.

In our definition, a “pair mode” is the alignment of a pair of neighboring MA^+ ions. From the 14 dipole directions shown in Fig. 1 we can derive $14^2 = 196$ pair modes. However, this number can be significantly reduced to 25 by considering only symmetry inequivalent modes, since many modes can be transformed into each other. The 25 inequivalent modes are listed in Fig. 2. Figure 3 shows an example of transformations among several equivalent modes. We will discuss our supercell models in terms of the pair modes listed in Fig. 2 hereafter.

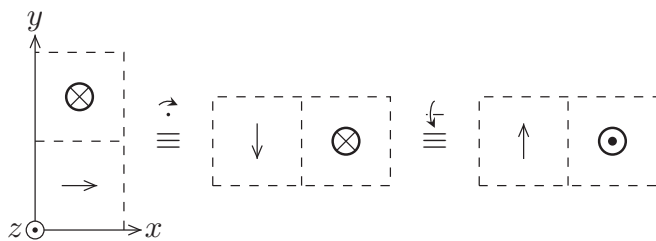


FIG. 3. Conversion of an arbitrary pair mode (left) into mode 25 (right) via a series of symmetry operations: rotation around $-z$ for 90° then rotation around x for 180° .

Specifically, modes 1–6 and 11–13 are constructed by two diagonal dipoles, modes 7–10 and 14–17 by one diagonal and one face-to-face dipole, and modes 18–25 by two face-to-face dipoles. In this paper we will only discuss dipoles with “strict” face-to-face orientations. Pair modes resulting from dipoles that deviate from the face-to-face line by the angle found in our previous work [32] are presented in Sec. S1 of Ref. [59].

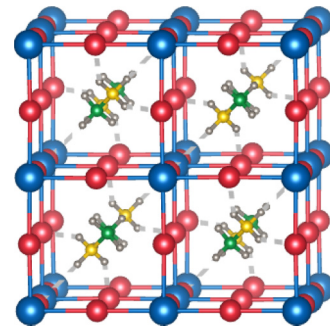


FIG. 4. An optimized $2 \times 2 \times 2$ supercell structure in which all MA^+ cations are oriented diagonally. The hydrogen bonds between I^- anions and H atoms in the $-\text{NH}_3^+$ group are highlighted by gray dashed lines.

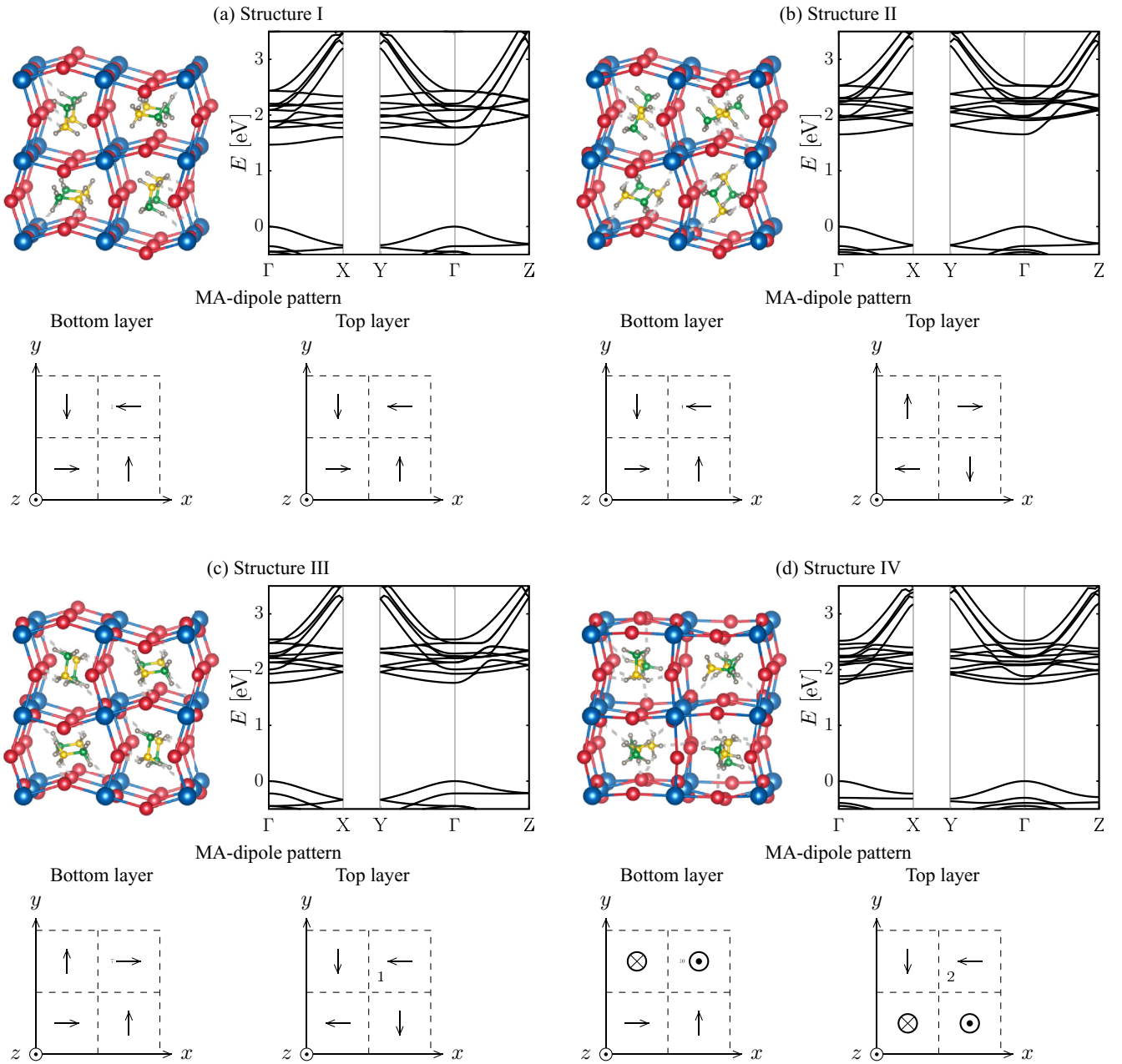


FIG. 5. Four optimized $2 \times 2 \times 2$ supercell structures I, II, III, and IV (in the upper-left panels) in which all MA^+ cations are oriented approximately face-to-face. For each system, the band structure (in the upper-right panel) as well as the patterns of MA dipoles (in the lower panel) in the bottom ($0 < z < 0.5$) and top ($0.5 < z < 1$) layers of the unit cell (bottom panels) are also shown.

B. Properties of optimized $2 \times 2 \times 2$ supercell models

1. General properties analysis based on dipole-direction distribution

In our previous primitive-cell study we found only two stable structures [32], as alluded to before. For $2 \times 2 \times 2$ supercell models, the situation changes dramatically. There are many possible alignments of MA dipoles in the initial structures. The optimization of them using the aforementioned DFT approach results in different atomic geometries corresponding to different local total-energy minima. Here we first select from the many local minima and structures that we found the

nonpolar structures, in which the vector sum of MA-dipole moments (approximately) vanishes.

Figure 4 shows a geometry optimized $2 \times 2 \times 2$ supercell in which all MA^+ ions are oriented diagonally. The C–N bonds are aligned parallel and alternately point in opposite directions. This results in a nearly vanishing net dipole moment in the supercell: the three components of the average dipole-moment vector are 0.001, 0.004, and 0.003 p_0 .

Figure 5 shows four optimized $2 \times 2 \times 2$ supercells, in which all MA^+ cations are oriented face-to-face. Also shown are their band structures along three high-symmetry lines Γ -X, Γ -Y, and Γ -Z around the band gap (for band structures along

TABLE I. Geometry parameters and properties of PBE+vdW optimized $2 \times 2 \times 2$ supercell structures I, II, III, and IV. Listed are lattice parameters (in Å), average MA⁺ dipole moment (in p_0), patterns of MA dipoles in the unit cell, distribution of MA-dipole directions, pair-mode distribution, relative total energy (in meV per unit MAPbI₃), and band gap (in eV).

Structure	Lattice parameters	Average MA ⁺ dipole moment	Bottom-layer pattern	Top-layer pattern	Dipole-direction distribution	Pair-mode distribution	Relative total energy	Band gap
I	$a = 12.28$ $b = 12.28$ $c = 12.68$	$ p_x = 0.003$ $ p_y = 0.000$ $ p_z = 0.195$			$2 + x, 2 - x$ $2 + y, 2 - y$	8 modes No. 20 8 modes No. 22 8 modes No. 23	112	1.469
II	$a = 12.26$ $b = 12.24$ $c = 12.71$	$ p_x = 0.001$ $ p_y = 0.002$ $ p_z = 0.008$			$2 + x, 2 - x$ $2 + y, 2 - y$	8 modes No. 20 8 modes No. 22 8 modes No. 24	23	1.654
III	$a = 12.24$ $b = 12.24$ $c = 12.62$	$ p_x = 0.001$ $ p_y = 0.000$ $ p_z = 0.008$			$2 + x, 2 - x$ $2 + y, 2 - y$	8 modes No. 20 8 modes No. 22 8 modes No. 24	0	1.762
IV	$a = 12.55$ $b = 12.24$ $c = 12.38$	$ p_x = 0.003$ $ p_y = 0.017$ $ p_z = 0.012$			$1 + x, 1 - x$ $1 + y, 1 - y$ $2 + z, 2 - z$	8 modes No. 20 8 modes No. 22 4 modes No. 24 4 modes No. 25	63	1.745

more high-symmetry lines please refer to Sec. S2 of Ref. [59]. Corresponding key parameters of these structures (e.g., relative stability, band gap) are listed in Table I. Structure III [Fig. 5(c)] is the most stable one as it corresponds to the lowest total energy among them. We set its total energy to 0 hereafter. The total energy of structures I [Fig. 5(a)], II [Fig. 5(b)], and IV [Fig. 5(d)] are 898, 182, and 500 meV per unit cell, or 112, 23, and 63 meV per MAPbI₃, respectively. The total energy of the structure shown in Fig. 4 is 170 meV per MAPbI₃, much higher than structures I–IV. Following the analysis of our previous work [32], this can be rationalized by the occurrence of diagonally oriented MA⁺ ions. These diagonally oriented dipoles prevent the inorganic framework from releasing energy by deforming the inorganic cage, which leads to a significantly higher total energy. It is thus unlikely that many diagonally oriented dipoles occur in MAPbI₃, which is also confirmed by our supercell calculations. Therefore we only focus on structures I–IV hereafter, in which only face-to-face MA⁺ ions are involved. Some structural parameters and the band structure of the systems shown in Fig. 4 are given in Sec. S3 of Ref. [59].

For each optimized supercell structure, we illustrate the MA-alignment “pattern” in both Fig. 5 and Table I. These patterns show that in structures I–III the MA⁺ cations are (approximately) located within the xy plane and regularly aligned. For the properties of each of these systems, we therefore observe an equivalence between the x and y directions, whereas the z direction exhibits differences. For example, the lattice parameters a and b are approximately equal, whereas c differs (cf. Table I). This equivalence is also reflected in the band structures [see Figs. 5(a)–5(c), upper-right panels]: for each system, the band structures in the Γ - X and Γ - Y directions are identical, while Γ - Z shows a different band dispersion.

Conversely, in structure IV the MA dipoles are oriented along the six different face-to-face directions $\pm x$, $\pm y$, and $\pm z$. The MA⁺ alignment exhibits a quasirandom character and no equivalence between any two directions can be observed. This results in different lattice parameters a , b , and c . However, the root-mean-square deviation of $\{a, b, c\}$ of structure IV is 0.13 Å, clearly smaller than structures I (0.19 Å), II (0.22 Å), and III (0.18 Å). In addition, Fig. 5(d) shows that the band structures of structure IV along Γ - X , Γ - Y , and Γ - Z are generally similar.

2. Pair-mode analysis

In the previous section we discussed the lattice parameters and band structures of four characteristic $2 \times 2 \times 2$ supercell models in terms of their dipole distribution. Now we analyze their total energies and band gaps in terms of pair modes. Figure 5 shows the dipole pattern for each geometry in the notation established in Fig. 1 (also listed in the fourth and fifth columns of Table I).

For a $2 \times 2 \times 2$ supercell model, each MA⁺ has six nearest neighbors, thus there are altogether $\frac{1}{2} \cdot 6 \cdot 2^3 = 24$ pair modes after eliminating double counting. Since all dipoles in these four systems are oriented along face-to-face directions, only modes 18–25 will contribute. Specifically, in modes 18, 19 and 21, the two dipoles are (approximately) linearly aligned; modes 20 and 22 include two vertical dipoles; modes 23 and 24 two parallel dipoles; and the two dipoles in mode 25 are

TABLE II. Relative geometry of dipoles in pair modes 18–25 defined in Fig. 2.

Mode No.	Dipole-dipole geometry
18	linear, extending
19	linear, head-to-head
20	vertical, in-plane
21	linear, tail-to-tail
22	vertical, in-plane
23	parallel
24	antiparallel
25	vertical, out-of-plane

orthogonal to each other and not located in the same plane. These geometric characteristics are summarized in Table II.

In structure I, II, or III, the orientation of dipoles within a layer (i.e., with similar z coordinate) alternates between x and y . This results in eight pair modes of type 20 and eight modes of type 22 (these two different “vertical” modes, in which the two dipoles are vertical and approximately in-plane, appear in pairs due to the periodic boundary conditions for $2 \times 2 \times 2$ supercell models). As a result, these three systems exhibit similar geometric properties as alluded to in the previous section.

However, both the total energy and band gap of structure I are significantly different from those of structures II and III, which we attribute to the difference in the remaining pair modes. In structures II and III, the dipoles in the “bottom” and the “top” layers are oriented in opposite directions, introducing eight antiparallel modes (No. 24). This similarity leads to similar band gaps (difference ~ 0.1 eV) and relatively close total energies (difference ~ 20 meV per unit MAPbI₃). In contrast, in structure I, the identical alignment in these two layers results in eight parallel modes (No. 23). The significantly higher total energy (> 100 meV per unit) suggests that mode 23, in which the two dipoles are aligned parallel, is less favorable than mode 24 that contains two antiparallel dipoles. In addition, the occurrence of the parallel mode also gives rise to a smaller band gap (by ~ 0.3 eV compared to structure III). Our results for structures I–III suggest a correlation between the stability of hybrid perovskites and the size of the band gap, that is, the higher the stability the larger the band gap. This observation agrees well with the trend reported by a recent experimental-theoretical study [60].

Despite the apparently different dipole-direction distribution, structure IV has a similar although not identical pair-mode distribution compared to structure III. The three-dimensional dipole-network results in eight pair modes of type 20, eight modes of type 22, four modes of type 24, and four modes of type 25. Hence, the major difference arises from the presence of mode 25, in which the two dipoles are approximately vertical and not located within the same plane. Our DFT results give a moderately higher total energy for structure IV (~ 60 meV per unit) and a band gap that is very close to that of structure III. This suggests that mode 25 does not significantly reduce the overall stability of the system.

Recapping the pair-mode distribution in $2 \times 2 \times 2$ supercell models: The in-plane vertical modes 20 and 22 are abundant. The antiparallel mode 24 can significantly stabilize the system,

whereas mode 25 decreases stability. The parallel mode 23 is energetically unfavorable. The linear modes 18, 19, and 21 are not present in structures I–IV.

C. Pair-mode distribution in optimized $4 \times 4 \times 4$ supercell structures

1. Reference structures and dipole distributions

In this section we discuss the DFT (PBE+vdW) results for a series of $4 \times 4 \times 4$ MAPbI₃ supercell models. Our objective is to generate snapshots of the cubic (high-temperature) MAPbI₃ phase, in which the MA⁺ ions are disordered. We therefore fixed the lattice parameters to $a = b = c = 25.25 \text{ \AA}$ for the $4 \times 4 \times 4$ supercells. This value corresponds to four times 6.31 \AA —the experimental lattice parameter of the cubic phase [7].

The atomic positions in the $4 \times 4 \times 4$ supercell models were randomly initialized using the following protocol:

(i) The C–N bond midpoint of each MA⁺ ion was located at the center of each single cell.

(ii) For each MA⁺, the direction of C–N bond and the axial rotational angle of the ion around the C–N bond was randomly set.

(iii) The initial PbI₃[−] framework is undeformed.

For each initial structure, we calculated the total electrostatic dipole-dipole interaction energy $E_{\text{init}}^{\text{dd}}$ by summing the interaction energy of each dipole pair. We used $p_0 = 2.2 \text{ D}$ and a dielectric constant of 25.7 [53] in this paper. The electrostatic energy is fast to compute and allows us to sample many thousands of $4 \times 4 \times 4$ models to generate an energy distribution as shown in Fig. 6(a). The distribution is of Gaussian character centered at 0. Due to the small dipole moment of each MA dipole and the large dielectric constant, the distribution width is quite small ($\sim 0.4 \text{ meV per MA dipole}$).

We randomly selected 33 initial structures from Fig. 6(a) in this paper. The distribution of their single-point total energies (centered at their mean value), as plotted in Fig. 6(b), exhibits a quasi-Gaussian character with a much larger width ($\sim 10 \text{ meV per MA}^+$) than Fig. 6(a). In addition, there is no clear correlation between the electrostatic-energy and total-energy sequence in these model systems. These results tell us that the electrostatic dipole-dipole interaction energy has only a minor contribution to the total energy. This implies that previously proposed large-scale simulation models based on the dipole-dipole interaction energy, such as the classical Monte Carlo approaches in Refs. [34,35], would erroneously overemphasize the electrostatic interaction energy.

For the DFT-optimized structures of these 33 samples, we plot the distribution of total energies in Fig. 6(c). This distribution is somewhat broader than Fig. 6(b) ($\sim 15 \text{ meV}$). Figures 7(a) and 7(b) show the optimized structures that have the highest and lowest total energies, respectively. Their difference is only 20 meV per MAPbI₃ unit, which is very small compared to the total-energy difference among the $2 \times 2 \times 2$ supercell models discussed in the previous section. We can therefore use these 33 optimized structures to properly represent the many possibilities of the disordered structure of the cubic (high-temperature) MAPbI₃ phase.

We observe three common features in the optimized structures of these 33 model systems [Figs. 7(a) and 7(b) as two ex-

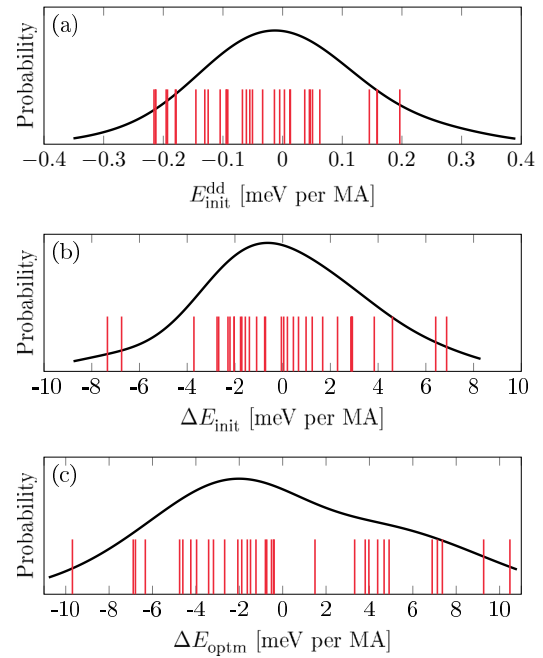


FIG. 6. Distribution of (a) electrostatic dipole-dipole interaction energy of the initial structures, (b) total energy of the initial structures, and (c) total energy of the DFT (PBE+vdW) optimized structures of the 33 $4 \times 4 \times 4$ supercell models (red vertical lines). In (b) and (c) the energies are shifted so that their respective mean values are 0. The black curve in (a) shows the probability distribution of the total dipole-dipole interaction energy obtained from 10^5 samples. The black curves in (b) and (c) show the energy distribution calculated from the 33 data points indicated by the red lines. All energies are given in meV per MAPbI₃ unit.

amples]. First, the average dipole moments are small (data not shown), thus they can be considered approximately nonpolar. Second, most of the MA dipoles, which were fully randomly initialized, were reoriented into face-to-face directions in the DFT-optimized structures. Third, they exhibit noticeable inorganic-framework deformation, which is irregular and local, and occurs along all three lattice vectors. This is very different to the deformation patterns in the ordered $2 \times 2 \times 2$ structures shown in Figs. 5(a)–5(c) (they are periodically extended within parallel lattice planes). The average octahedron-tilting angle is 11.2° , clearly smaller than the (in-plane) tilting angles in Figs. 5(a)–5(c) (ranging between 15.5° and 16.9°), as well as the average tilting angle in the irregular structure Fig. 5(d) (14.5°). Figure 8 shows that there is a rough correlation between the larger average tilting angle and the lower total energy within these 33 optimized cubic supercell structures.

In these 33 model systems, the total energy of the relaxed structures is on average 225 meV per MAPbI₃ unit lower than that of the initial structures. The contribution to this total-energy minimization, as we understand, consists of two major components: the formation of hydrogen bonds (40–50 meV per bond, thus 120–150 meV for three bonds [28,29,31,32]), and the inorganic-cage deformation. Estimated in this way, the latter contribution is much larger than the $\sim 20 \text{ meV per unit MAPbI}_3$ (with an average deformation angle of 5.4°)

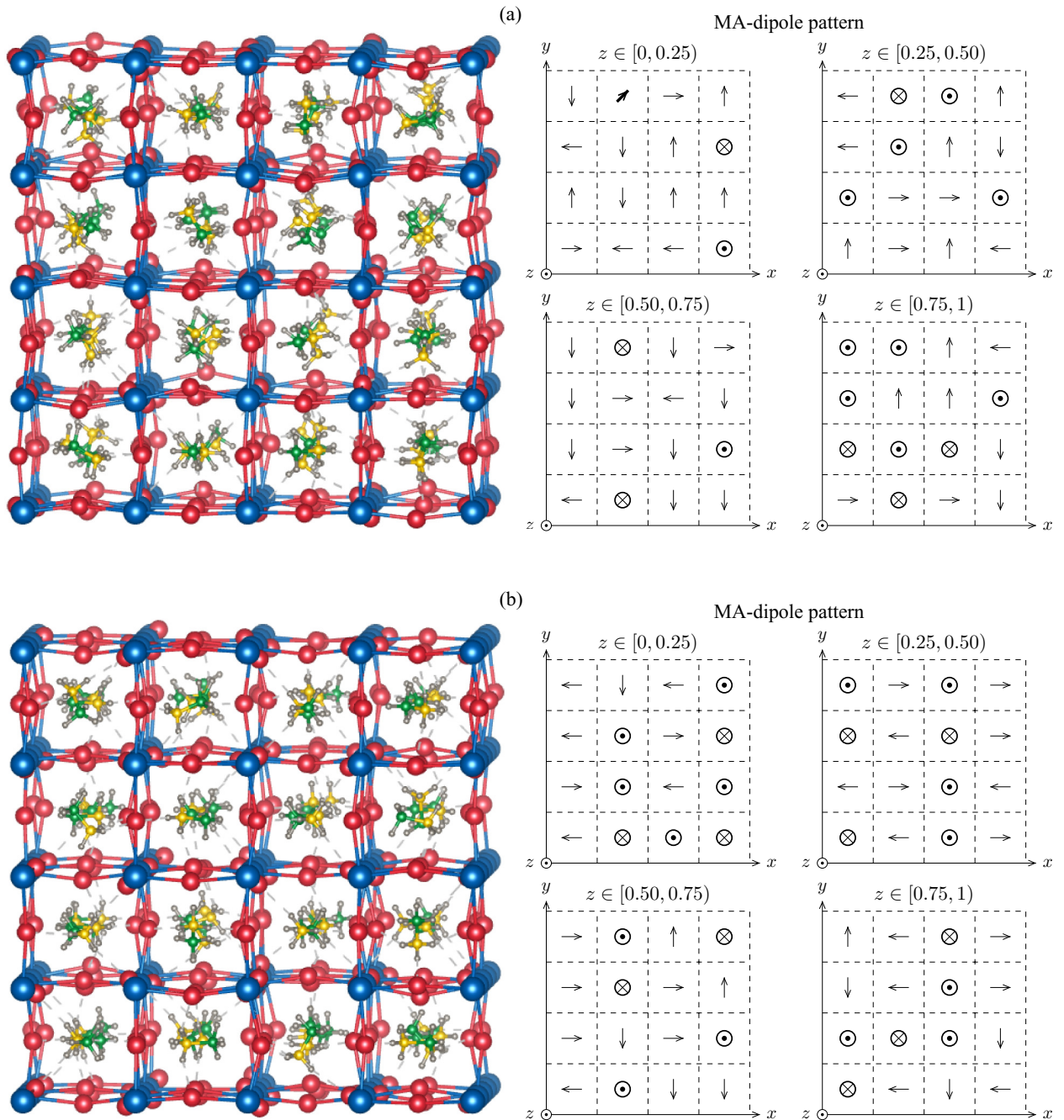


FIG. 7. Two optimized structures of $4 \times 4 \times 4$ supercell models and their MA-dipole patterns within xy layers of different z ranges. (a) Highest-energy structure and (b) Lowest-energy structure.

reported in our previous primitive-cell study [32]. This can be rationalized by the much larger average tilting angle (11.2°) in the optimized $4 \times 4 \times 4$ structures. Most of the MA dipoles (a) are properly bound to the inorganic framework and (b) adopt the (quasi-)face-to-face direction in the optimized structures as alluded to earlier. We therefore argue that the difference in total energies among the 33 DFT-relaxed structures is mainly due to different alignments of MA dipoles which result in different magnitudes and shapes of inorganic-framework deformation.

2. Pair-mode analysis

To understand the final dipole alignments we make use of our pair-mode concept. Here we first analyze the pair-mode distribution of the optimized structures with the highest [Fig. 7(a)] and lowest [Fig. 7(b)] total energies. Their dipole patterns in different xy layers (the z coordinates of MA^+ ions are similar within the same layer) are plotted in Fig. 7. Table III summarizes the distribution of altogether $\frac{1}{2} \cdot 6 \cdot 4^3 = 192$ modes in each structure.

Four aspects characterize the pair-mode distributions:

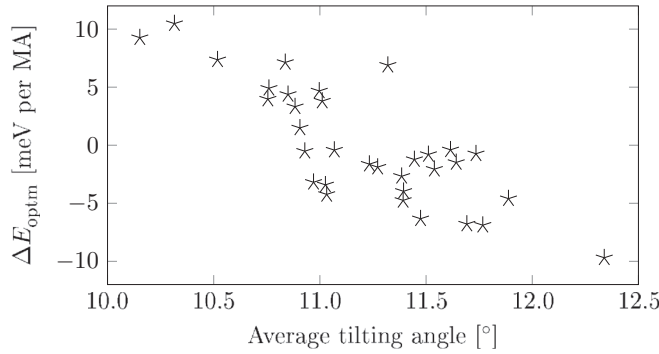


FIG. 8. Relative total energy (per unit MAPbI₃) vs the average octahedron-tilting angle of each optimized $4 \times 4 \times 4$ supercell structure.

(1) Diagonal dipoles are very rare: only 1 in Fig. 7(a), resulting in six pair modes in the mode 1–17 category. All other dipoles are distributed over all six face-to-face directions $\pm x$, $\pm y$, and $\pm z$, similar to structure IV of $2 \times 2 \times 2$ supercell model discussed previously.

(2) Vertical modes, especially the in-plane modes 20 and 22, dominate in both structures. The out-of-plane mode 25 is of nearly equal importance in Fig. 7(a), while in Fig. 7(b) it is less frequent.

(3) The only noticeable distribution of linear modes is 18 in Fig. 7(a) ($13/192 = 0.068$).

(4) The two parallel modes are equally distributed in Fig. 7(a), while in Fig. 7(b) the antiparallel mode 24 is significantly more populated than 23.

To summarize, the lowest-energy structure [Fig. 7(b)] exhibits much higher distribution in pair modes 20 and 22, nearly no population in linear modes, and obvious importance in mode 24 over 23.

To quantify the pair-mode pattern, we generate a pair-mode distribution from the 33 considered samples in this work. Figure 9(a) shows the pair-mode distribution of each sample as a heat map, and Fig. 9(b) shows the overall pair-mode distribution of all 33 samples (altogether $33 \cdot \frac{1}{2} \cdot 6 \cdot 4^3 = 6336$

TABLE III. Pair-mode distribution of optimized $4 \times 4 \times 4$ supercell models shown in Figs. 7(a) and 7(b).

Mode No.	Fig. 7(a) (highest energy)	Fig. 7(b) (lowest energy)
Diagonal-dipole containing pair modes		
1–17	6	0
Linear modes		
18	13	2
19	3	1
21	2	3
Vertical modes		
20	42	60
22	44	56
25	40	22
Parallel modes		
23	21	17
24	21	31

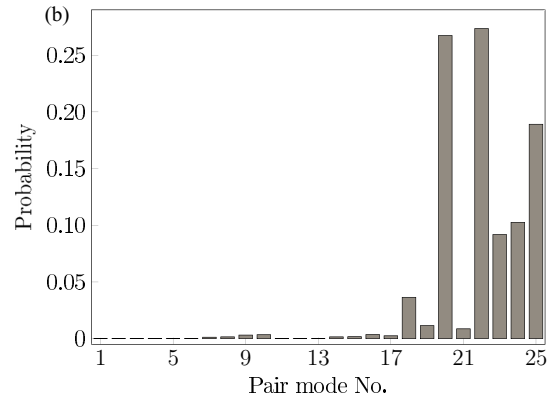
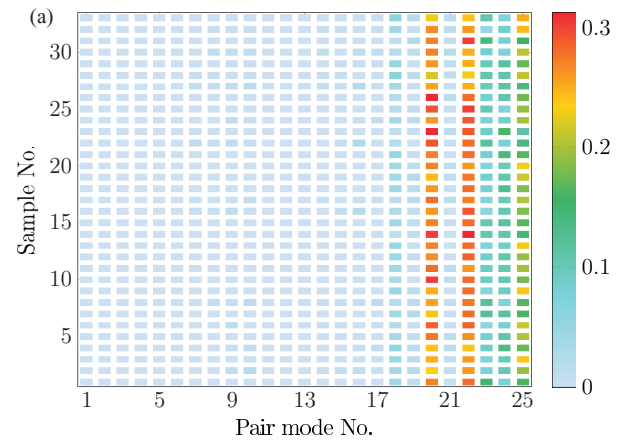


FIG. 9. Pair-mode distribution of optimized $4 \times 4 \times 4$ supercell models: (a) distribution of each individual sample, and (b) the overall distribution of all samples.

modes). Figure 9(a) indicates that the pair-mode distributions associated with all samples are similar. In general, the population of all pair modes that involve one or two diagonal dipoles, i.e., Nos. 1–17, is negligible. This indicates that the probability to find a diagonally oriented MA⁺ cation in the relaxed disordered cubic structure is very low, in good agreement with the *ab initio* MD results of polar-angle distribution of MA⁺ ions [41]. The vertical modes 20, 22, and 25, especially the in-plane modes 20 and 22, are the most dominant. The parallel 23 and antiparallel 24 modes are also noticeably distributed and they have almost equal population. Finally, the population of the linear modes 18, 19, and 21 is small. The occurrence of the head-to-head 19 and tail-to-tail 21 modes is almost negligible.

The pair-mode distribution shown in Fig. 9 enables us to construct large MAPbI₃ models that are out of reach of DFT. Since such large models follow the MA distribution in stable configurations and include MA⁺ nearest-neighbor interactions, they will provide good models to study realistic MAPbI₃ structures under realistic conditions. The construction of such large multiscale MAPbI₃ models will be the subject of future work [61].

To better understand the pair-mode distribution in Fig. 9, we focus on the modes 18–25. For an arbitrary face-to-face dipole, the possibilities to construct different pair modes with another face-to-face nearest neighbor are different. For example, there are two ways to construct mode 18 [Fig. 10(a)]

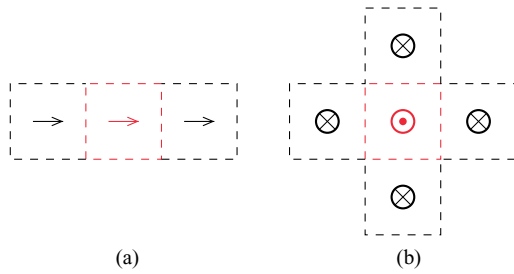


FIG. 10. Possibilities to construct pair mode (a) 18 and (b) 24 for a face-to-face dipole (colored in red) with its nearest neighbors (colored in black).

and four ways for 24 [Fig. 10(b)]. Table IV lists the number of possibilities and the corresponding probabilities (i.e., number of possibilities divided by $6 \cdot 6 = 36$). These *probabilities* refer to *fully random* systems, in which the dipoles are (a) oriented along face-to-face directions and (b) not interacting with each other (i.e., neither electrostatically nor via cage deformation). From the DFT results, we can then extract the probabilities in the relaxed structures associated with these modes that take the full electrostatic and structural response into account. We define these probabilities as the number of times a mode occurs in the 33 samples divided by the total number of modes in the $4 \times 4 \times 4$ supercell models (6336). The resulting probabilities are also listed in Table IV and enable a direct comparison between noninteracting dipoles and the real systems.

We start from the vertical modes 20, 22, and 25. They are the highest populated modes in fully random systems thus can be understood as “intrinsically” dominant modes. In relaxed structures, there are significant increases in the distribution in both in-plane modes 20 (0.045, namely 20.3%) and 22 (0.051 or 23.1%). In contrast, a noticeable drop (0.033 or 14.9%) can be observed in the DFT results for the out-of-plane mode 25. For the least populated linear modes, the MA-pair interaction results in a 0.019 (34.4%) drop for mode 18, and a more significant decrease in the population in both modes 19 and 22 (the distribution in these two modes almost vanish in the optimized structures). Finally, the distribution in both parallel

TABLE IV. Number of possibilities and probability to construct a pair mode (from 18 to 25) for an arbitrary dipole in a system in which all dipoles are fully randomly distributed in six face-to-face directions, as well as the probability of this mode in the 33 investigated relaxed $4 \times 4 \times 4$ supercell models.

Mode No.	Number of possibilities	Probability in fully random systems	Probability in relaxed systems
18	2	0.056	0.036
19	1	0.028	0.012
20	8	0.222	0.267
21	1	0.028	0.009
22	8	0.222	0.274
23	4	0.111	0.092
24	4	0.111	0.103
25	8	0.222	0.189

TABLE V. Pair-mode energies (in meV) of modes 18, 20, and 22–25 calculated by fitting Eq. (3.1).

Mode No. (n)	Pair-mode energy (E_n)
18	52.9
20	0
22	6.8
23	49.9
24	24.5
25	31.9

(No. 23) and antiparallel (No. 24) modes are nearly identical and slightly lower than the theoretical values.

3. Pair-mode expansion of the total energy

We can now use the dominant modes in Table IV, i.e., modes 18, 20, and 22–25, to perform a mode expansion of the total energy of a supercell structure:

$$E_{\text{optm}} = \sum_n p_n E_n + \text{const}, \quad n \in \{18, 20, 22, 23, 24, 25\}. \quad (3.1)$$

Here n labels the pair modes, p_n is the probability of the n th mode (last column of Table IV), and E_n is the associated “pair-mode energy.” Using Eq. (3.1) to fit the total-energy and pair-mode-distribution data, we obtained the set of E_n listed in Table V. We use the constant term in Eq. (3.1) to shift the smallest pair-mode energy value, i.e., E_{20} , to 0. The resulting pair-mode energies agree reasonably well with our analysis of the pair-mode distribution, and can give us an estimate of how the system will react to the change of an MA dipole from one face-to-face direction to another. For example, from modes 20 to 23, the system total energy will increase by ~ 50 meV. The root-mean-square error between the fitted and DFT-calculated energies is 3.0 meV per dipole, equivalently 1.0 meV per pair mode. The correspondence between the DFT and the fitted energies are given in Sec. S5 of Ref. [59].

Our results indicate that, in MAPbI_3 , the interaction between the neighboring MA^+ ions favors the in-plane vertical modes 20 and 22. The prevalent population of these two modes (together with the out-of-plane vertical mode 25) causes a three-dimensional isotropy on a large length scale, which effectively makes the material cubic. Conversely, the vanishing population in the linear modes (No. 18, especially Nos. 19 and 21) strongly limits the formation of linearly aligned neighboring MA^+ ions. This is very different to the formation of long linear MA chains predicted by the combination of *ab initio* MD and classical Monte Carlo simulations based on purely electrostatic interactions [34,35].

4. Angular distribution of dipoles

So far we have limited our discussion to discrete MA-dipole angles (0° , 90° , and 180°). In reality, the angle varies continuously between 0° and 180° . From the DFT-optimized $4 \times 4 \times 4$ structures we extracted the angle between each pair of nearest-neighbor MA dipoles. The distribution of this angle

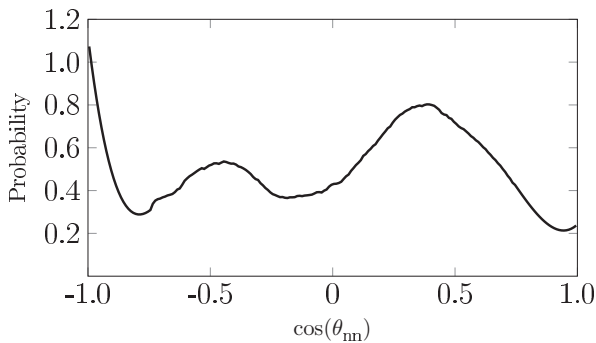


FIG. 11. Distribution of the cosine function of θ_{mn} (the angle between two nearest-neighbor MA dipoles) averaged over all 33 optimized $4 \times 4 \times 4$ supercell structures.

(plotted in Fig. 11) is similar to the previous *ab initio* MD results [41]. Here we briefly discuss the three characteristic features of the distribution:

- (1) 180° (cosine = -1), corresponding to pair modes 19, 21, and 24: the distribution exhibits a sharp peak, since only population in 24 is noticeable and the two dipoles tend to take nearly perfect antiparallel alignment.
- (2) 0° (cosine = 1), modes 18 and 23: in many cases the two dipoles form an angle (up to $\sim 45^\circ$) instead of being aligned perfectly in one direction, thus resulting in a broad distribution.
- (3) 90° (cosine = 0): the most populated modes 20, 22, and 25 are all included in the large region of ($\sim 45^\circ, \sim 135^\circ$).

IV. CONCLUSIONS

We have studied a series of MAPbI₃ supercell models using DFT. To establish a multiscale model, we derived and analyzed the concept of pair modes, i.e., the interaction of nearest MA-ion pairs. We first investigated several small $2 \times 2 \times 2$ supercell models, in which we can cancel out the overall dipole moment by hand using suitable dipole orientations. Our DFT results indicate that differences in pair modes have a significant effect on the atomic and electronic structure of these

models. This finding motivated our exploration into larger $4 \times 4 \times 4$ MAPbI₃ supercell models, which we used to simulate disordered MAPbI₃ structures by randomly initializing the MA⁺ orientations. Structural optimization using DFT and our pair-mode analysis reveal that the final locations of MA⁺ ions is not fully random, but follows certain preferred orientations that depend on the surrounding. Our results indicate that vertical geometries are preferred for nearest MA pairs, which will lead to the formation of a three-dimensional isotropic network of MA dipoles. In contrast, linearly extended MA pairs in neighboring cells are largely suppressed.

The discussion of pair modes and their distribution in this paper is based on a series of (meta)stable configurations of disordered MAPbI₃. DFT is an appropriate tool for this purpose as it can predict the geometries and give a reliable estimation of total energies of these configurations. We can use this dipole distribution to build a multiscale model to generate the local structure in bulk MAPbI₃ samples on large length scales, e.g., of a few tens of single cells [61]. The fitted pair-mode energies obtained in this work and the energy barriers for an MA dipole to change its direction calculated in our other works using DFT [28,29] allow us to include temperature in this multiscale modeling scheme.

ACKNOWLEDGMENTS

We thank H. Levard as well as M. Bokdam and J. Lahnsteiner for fruitful discussions. The generous allocation of computing resources by the CSC-IT Center for Science (via the Project No. ay6311) and the Aalto Science-IT project are gratefully acknowledged. An award of computer time was provided by the Innovative and Novel Computational Impact on Theory and Experiment (INCITE) program. This research used resources of the Argonne Leadership Computing Facility, which is a DOE Office of Science User Facility supported under Contract DE-AC02-06CH11357. This work was supported by the Academy of Finland through its Centres of Excellence Programme (2012-2014 and 2015-2017) under Project No. 251748 and No. 284621, as well as its Key Project Funding scheme under Project No. 305632.

-
- [1] H. J. Snaith, *J. Phys. Chem. Lett.* **4**, 3623 (2013).
 - [2] M. A. Green, A. Ho-Baillie, and H. J. Snaith, *Nat. Photon.* **8**, 506 (2014).
 - [3] <https://www.nrel.gov/pv/assets/images/efficiency-chart.png> (National Renewable Energy Laboratory: Best research-cell efficiencies, 2016).
 - [4] H.-S. Kim, C.-R. Lee, J.-H. Im, K.-B. Lee, T. Moehl, A. Marchioro, S.-J. Moon, R. Humphry-Baker, J.-H. Yum, J. E. Moser *et al.*, *Sci. Rep.* **2**, 591 (2012).
 - [5] M. M. Lee, J. Teuscher, T. Miyasaka, T. N. Murakami, and H. J. Snaith, *Science* **338**, 643 (2012).
 - [6] P. Jackson, R. Wuerz, D. Hariskos, E. Lotter, W. Witte, and M. Powalla, *Phys. Status Solidi Rapid Res. Lett.* **10**, 583 (2016).
 - [7] C. C. Stoumpos, C. D. Malliakas, and M. G. Kanatzidis, *Inorg. Chem.* **52**, 9019 (2013).
 - [8] S. de Wolf, J. Holovsky, S.-J. Moon, P. Löper, B. Niesen, M. Ledinsky, F.-J. Haug, J.-H. Yum, and C. Ballif, *J. Phys. Chem. Lett.* **5**, 1035 (2014).
 - [9] S. D. Stranks, G. E. Eperon, G. Grancini, C. Menelaou, M. J. P. Alcocer, T. Leijtens, L. M. Herz, A. Petrozza, and H. J. Snaith, *Science* **342**, 341 (2013).
 - [10] G. Xing, N. Mathews, S. Sun, S. S. Lim, Y. M. Lam, M. Grätzel, S. Mhaisalkar, and T. C. Sum, *Science* **342**, 344 (2013).
 - [11] C. S. Ponseca, Jr., T. J. Savenije, M. Abdellah, K. Zheng, A. Yartsev, T. Pascher, T. Harlang, P. Chabera, T. Pullerits, A. Stepanov *et al.*, *J. Am. Chem. Soc.* **136**, 5189 (2014).
 - [12] M. B. Johnston and L. M. Herz, *Acc. Chem. Res.* **49**, 146 (2016).
 - [13] H. J. Snaith, A. Abate, J. M. Ball, G. E. Eperon, T. Leijtens, N. K. Noel, S. D. Stranks, J. T.-W. Wang, K. Wojciechowski, and W. Zhang, *J. Phys. Chem. Lett.* **5**, 1511 (2014).

- [14] H.-S. Kim, I.-H. Jang, N.-Y. Ahn, M.-S. Choi, A. Guerrero, J. Bisquert, and N.-G. Park, *J. Phys. Chem. Lett.* **6**, 4633 (2015).
- [15] B. Chen, M. Yang, S. Priya, and K. Zhu, *J. Phys. Chem. Lett.* **7**, 905 (2016).
- [16] J.-H. Noh, S.-H. Im, J.-H. Heo, T. N. Mandal, and S.-I. Seok, *Nano Lett.* **13**, 1764 (2013).
- [17] G. Niu, W. Li, F. Meng, L. Wang, H. Dong, and Y. Qiu, *J. Mater. Chem. A* **2**, 705 (2014).
- [18] G. Niu, X. Guo, and L. Wang, *J. Mater. Chem. A* **3**, 8970 (2015).
- [19] A. Poglitsch and D. Weber, *J. Chem. Phys.* **87**, 6373 (1987).
- [20] M. T. Weller, O. J. Weber, P. F. Henry, A. M. di Pumpo, and T. C. Hansen, *Chem. Commun.* **51**, 4180 (2015).
- [21] D. A. Egger, A. M. Rappe, and L. Kronik, *Acc. Chem. Res.* **49**, 573 (2016).
- [22] R. E. Wasylshen, O. Knop, and J. B. MacDonald, *Solid State Commun.* **56**, 581 (1985).
- [23] A. A. Bakulin, O. Selig, H. J. Bakker, Y. L. A. Rezus, C. Müller, T. Glaser, R. Lovrincic, Z. Sun, Z. Chenn, A. Walsh, J. M. Frost, and T. L. C. Jansen, *J. Phys. Chem. Lett.* **6**, 3663 (2015).
- [24] T. Chen, B. J. Foley, B. Ipek, M. Tyagi, J. R. D. Copley, C. M. Brown, J. J. Choi, and S.-H. Lee, *Phys. Chem. Chem. Phys.* **17**, 31278 (2015).
- [25] S. Meloni, T. Moehl, W. Tress, M. Franckevičius, M. Saliba, Y. H. Lee, P. Gao, M. K. Nazeeruddin, S. M. Zakeeruddin, U. Rothlisberger, and M. Grätzel, *Nat. Commun.* **7**, 10334 (2016).
- [26] E. Mosconi, C. Quarti, T. Ivanovska, G. Ruani, and F. de Angelis, *Phys. Chem. Chem. Phys.* **16**, 16137 (2014).
- [27] J.-H. Lee, N. C. Bristowe, P. D. Bristowe, and A. K. Cheetham, *Chem. Commun.* **51**, 6434 (2015).
- [28] J. Li, M. Bouchard, P. Reiss, D. Aldakov, S. Pouget, R. Demadrille, C. Aumaitre, B. Frick, D. Djurado, M. Rossi, and P. Rinke, *J. Phys. Chem. Lett.* (to be published).
- [29] J. Li and P. Rinke (unpublished).
- [30] N. Onoda-Yamamuro, T. Matsuo, and H. Suga, *J. Phys. Chem. Solids* **53**, 935 (1992).
- [31] D. A. Egger and L. Kronik, *J. Phys. Chem. Lett.* **5**, 2728 (2014).
- [32] J. Li and P. Rinke, *Phys. Rev. B* **94**, 045201 (2016).
- [33] J. M. Frost, K. T. Butler, F. Brivio, C. H. Hendon, M. van Schilfgaarde, and A. Walsh, *Nano Lett.* **14**, 2584 (2014).
- [34] J. M. Frost, K. T. Butler, and A. Walsh, *APL Mater.* **2**, 081506 (2014).
- [35] A. M. A. Leguy, J. M. Frost, A. P. McMahon, V. Garcia Sakai, W. Kochelmann, C. H. Law, X. Li, F. Foglia, A. Walsh, B. C. O'Regan *et al.*, *Nat. Commun.* **6**, 7124 (2015).
- [36] P. Umari, E. Mosconi, and F. de Angelis, *Sci. Rep.* **4**, 4467 (2014).
- [37] E. Menéndez-Proupin, P. Palacios, P. Wahnón, and J. C. Conesa, *Phys. Rev. B* **90**, 045207 (2014).
- [38] W. Yin, J. Yang, J.-G. Kang, Y. Yan, and S. Wei, *J. Mater. Chem. A* **3**, 8926 (2015).
- [39] F. Brivio, J. M. Frost, J. M. Skelton, A. J. Jackson, O. J. Weber, M. T. Weller, A. R. Goñi, A. M. A. Leguy, P. R. F. Barnes, and A. Walsh, *Phys. Rev. B* **92**, 144308 (2015).
- [40] I. Deretzis, B. N. di Mauro, A. Alberti, G. Pellegrino, E. Smecca, and A. la Magna, *Sci. Rep.* **6**, 24443 (2016).
- [41] J. Lahnsteiner, G. Kresse, A. Kumar, D. D. Sarma, C. Franchini, and M. Bokdam, *Phys. Rev. B* **94**, 214114 (2016).
- [42] J. Ma and L.-W. Wang, *Nano Lett.* **15**, 248 (2015).
- [43] This is a short notation for simplicity and does not mean that we treat an MA⁺ ion only as a dipole.
- [44] J. Even, M. Carignano, and C. Katan, *Nanoscale* **8**, 6222 (2016).
- [45] J. P. Perdew, K. Burke, and M. Ernzerhof, *Phys. Rev. Lett.* **77**, 3865 (1996).
- [46] A. Tkatchenko and M. Scheffler, *Phys. Rev. Lett.* **102**, 073005 (2009).
- [47] E. van Lenthe, E. J. Baerends, and J. G. Sneijders, *J. Chem. Phys.* **99**, 4597 (1993).
- [48] J. Even, L. Pedesseau, M.-A. Dupertuis, J.-M. Jancu, and C. Katan, *Phys. Rev. B* **86**, 205301 (2012).
- [49] J. Even, L. Pedesseau, J.-M. Jancu, and C. Katan, *J. Phys. Chem. Lett.* **4**, 2999 (2013).
- [50] F. Brivio, K. T. Butler, A. Walsh, and M. van Schilfgaarde, *Phys. Rev. B* **89**, 155204 (2014).
- [51] C. Katan, L. Pedesseau, M. Kepenekian, A. Rolland, and J. Even, *J. Mater. Chem. A* **3**, 9232 (2015).
- [52] F. Chiarella, A. Zappettini, F. Licci, I. Borriello, G. Cantele, D. Ninno, A. Cassinese, and R. Vaglio, *Phys. Rev. B* **77**, 045129 (2008).
- [53] F. Brivio, A. B. Walker, and A. Walsh, *APL Mater.* **1**, 042111 (2013).
- [54] V. Blum, R. Gehrke, F. Hanke, P. Havu, V. Havu, X. Ren, K. Reuter, and M. Scheffler, *Comput. Phys. Commun.* **180**, 2175 (2009).
- [55] V. Havu, V. Blum, P. Havu, and M. Scheffler, *J. Comput. Phys.* **228**, 8367 (2009).
- [56] S. V. Levchenko, X. Ren, J. Wierfink, R. Johanni, P. Rinke, V. Blum, and M. Scheffler, *Comput. Phys. Commun.* **192**, 60 (2015).
- [57] F. Knuth, C. Carbogno, V. Atalla, V. Blum, and M. Scheffler, *Comput. Phys. Commun.* **190**, 33 (2015).
- [58] See <http://dx.doi.org/10.17172/NOMAD/2018.05.05-1>.
- [59] See Supplemental Material at <http://link.aps.org/supplemental/10.1103/PhysRevB.98.045201> for individual MA dipoles and pair modes including the deviation from face-to-face directions; structural parameters and band structures of several $2 \times 2 \times 2$ supercells; pair-mode distribution from DFT results of $3 \times 3 \times 3$ supercells; correspondence between the fitted and DFT energies of relaxed $4 \times 4 \times 4$ supercell structures.
- [60] T. Baikie, Y. Fang, J. M. Kadro, M. Schreyer, F. Wei, S. G. Mhaisalkar, M. Grätzel, and T. J. White, *J. Mater. Chem. A* **1**, 5628 (2013).
- [61] J. Järvi, J. Li, and P. Rinke, [arXiv:1806.05560](https://arxiv.org/abs/1806.05560).